water

Article

Study on Part-Load Cavitation in High-Specific-Speed Centrifugal Pump

Zhenhua Shen [1], Chao Wang [1,*], Jinfeng Zhang [2], Shijun Qiu [3] and Rong Lin [3]

[1] Department of Mechanical and Mold Engineering, Taizhou Vocational College of Science and Technology, 288 Jiamu Road, Taizhou 318020, China; steve_szh@126.com
[2] Research Center of Fluid Machinery Engineering and Technology, Jiangsu University, 301 Xuefu Road, Zhenjiang 212013, China; zhangjinfeng@ujs.edu.cn
[3] Leo Group Pump (Zhejiang) Co., Ltd., No.1 3rd Street, Wenling 317500, China; qiushijun@leopump.com (S.Q.); linrong@leopump.com (R.L.)
* Correspondence: wangc1985@126.com; Tel.: +86-186-6221-8873

Abstract: Some high-specific-speed centrifugal pumps exhibit instability in terms of hydraulic performance and cavitation characteristics, and there's a lack of reliable numerical models to guide the optimization of cavitation instability. This paper, by conducting a study on mesh independence, analyzes the cavitation curves and cavitation counters for various mesh combinations in the numerical model, The findings indicate that the boundary layer grid not only influences the location of peak points but also the size of the peak. To achieve a stable NPSH peak position, the $y+$ at the blade leading edge of high-specific-speed centrifugal pumps needs to be controlled between 20–80. The turbulence model, evaporation coefficient, and condensation coefficient were simulated using the orthogonal experimental design method, analyzing the impact of these parameters on the NPSH peak. A visual high-speed photography test rig was established, and rotating cavitation and sheet cavitation is found at part-load. By comparing the cavitation and pressure counters with high-speed photography images, a numerical model was obtained that closely mirrors the experimental cavitation characteristics.

Keywords: high-specific-speed pump; part-load; cavitation instability; flow visualization; numerical model

Citation: Shen, Z.; Wang, C.; Zhang, J.; Qiu, S.; Lin, R. Study on Part-Load Cavitation in High-Specific-Speed Centrifugal Pump. *Water* **2024**, *16*, 2180. https://doi.org/10.3390/w16152180

Academic Editor: Helena M. Ramos

Received: 29 June 2024
Revised: 29 July 2024
Accepted: 30 July 2024
Published: 1 August 2024

1. Introduction

The pump cavitation performance is represented by the NPSH (net positive suction head). The larger the NPSH, the worse the cavitation performance. Some high-specific-speed pumps exhibit instability in hydraulic and cavitation performance [1,2]. This is especially true for cavitation instability at part-load, as indicated by the $\mathrm{NPSH}_{3\%}$ peak. The peak value indicates that the risk of cavitation at this flow point is increased.

Extensive research has been conducted by numerous scholars into the phenomenon of part-load cavitation, leveraging a combined approach of experimental and numerical simulation methods. A subset of these studies has focused on elucidating the unstable behaviors within the operational regime of pumps. For instance, Friedrichs [3] discovered, through experimental analysis, that under part-load conditions, the adoption of an increasing flow method results in instability in the head and peak point of $\mathrm{NPSH}_{3\%}$. Conversely, the flow curve obtained through a decreasing flow method exhibits stability. However, numerical calculations have revealed that the apparent smoothness of this curve is misleading, as the flow in the pressure drop region of the front cover plate is disrupted by separated flow. Deng [4–6] employed visualization techniques along with numerical simulations to conduct a rigorous examination of part-load conditions in screw centrifugal pumps. Their research uncovered that the low pressure within the vortex core, resulting from secondary flow through the rim gap, triggers backflow vortex cavitation. Notably, two distinct cavitation clouds were observed in this phenomenon, with the size of the cavitation clouds influenced by the extent of the backflow area. Chen Qi [7] delved into the characteristics of cavitation onset and progression in a centrifugal pump operating under part-load conditions. Their findings indicate that, in the absence of cavitation, there exists uneven recirculation at the suction surface of the blade and near the impeller outlet close to the tongue of the centrifugal pump. As cavitation progresses, the turbulence intensity at the impeller inlet initially increases and subsequently decreases, while the decrease in recirculation intensity leads to the attenuation of recirculation cavitation. Lastly, Shen [8] conducted a preliminary numerical-simulation-based exploration of the formation mechanism of part-load cavitation instability in high-specific-speed pumps, offering further insights into this complex phenomenon.

Investigating the unstable phenomena occurring at the pump inlet, Fu and Yuan [9–15] conducted extensive numerical simulation studies on the 65-50-160 pump model under part-load conditions, complementing their findings with experimental validations. Their results revealed the presence of a backflow area within the pump inlet, where a significant concentration of cavitation bubbles emerged near the vortex center, exhibiting periodic variations with the rotation of the pump. This phenomenon was identified as backflow vortex cavitation. Cui and Feng [16,17] delved into a wide range of unstable flow phenomena encountered in centrifugal pumps operating under part-load conditions, including impeller inlet backflow, rotating stall, flow separation, viscous wake, and clearance flow. Their comprehensive analysis provided valuable insights into these complex flow dynamics. Li [18] conducted a numerical simulation analysis to explore the internal flow characteristics of a centrifugal pump across different flow rates. Their findings highlighted the significance of inlet recirculation, which tended to obstruct the flow channel and induce vortex structures in the suction zone. This recirculation was identified as a critical factor contributing to the degradation of centrifugal pump performance. Similarly, the research conducted by Zhang and Zhou [19,20] emphasized the adverse effects of stall mass, which can block flow channels, reduce flow areas, and increase the flow in adjacent channels. This phenomenon often leads to significant fluctuations in the head, resulting in an unstable "saddle-type" performance curve for the pump. In order to decrease the risk of cavitation, many scholars have developed flow control techniques to minimize the unstable cavitation. Roohi, Mousavi and Alavi [21,22] studied the super-cavitation flow of the hydrofoil with a hybrid surface by utilizing the large eddy simulation (LES) turbulence model and Kunz mass transfer model, finding that the use of a superhydrophobic surface on the pressure side and trailing edge of a hydrofoil, along with a super-hydrophilic surface on the leading edge, can reduce the flow instability and delay the onset of cavitation.

In summary, the majority of scholarly research on part-load cavitation has been conducted through experimental means, revealing unstable phenomena such as recirculation cavitation, rotating cavitation, and rotating stall. Nevertheless, the exploration into the internal mechanisms of part-load cavitation remains insufficient, and there is currently a dearth of dependable numerical models to aid in the control and optimization of cavitation instability. Consequently, this study employs an experimental design approach to conduct numerical simulation investigations on turbulence models, evaporation coefficients, and condensation coefficients. Additionally, it examines the impact of various parameters on the NPSH peak. Furthermore, a high-speed photography test rig has been established, facilitating comparison between cavitation counters and high-speed photographic images.

2. Pump Model Test

2.1. Pump Model

In order to investigate the numerical modeling of part-load cavitation instability phenomena in high-specific-speed pumps, this study presents the design of a novel visual pump model based on the original model from [8] with the $NPSH_{3\%}$ peak at the 80% rated flow point. Table 1 outlines the principal parameters of the pump, which form the cornerstone of this investigation. The transparent pump casing is crafted from organic glass

(PMMA) and precision-machined using a state-of-the-art machining center. This casing boasts a transmittance exceeding 92%, enabling the comprehensive visualization of the internal flow dynamics.

Table 1. Main parameters of pump model.

Flow Rate (m^3/h)	Head (m)	Rotating Speed (rev/min)	Impeller Inlet Diameter	Impeller Outer Diameter (mm)	Impeller Outlet Width (mm)
90	7.7	2900	80.7	94.7–105.6	31.57

The impeller of the pump model is fabricated from stainless steel 316L, chosen for its superior mechanical properties and surface finish that closely resembles industrial-grade products. As depicted in Figure 1, the stainless-steel impeller is initially formed using 3D-printed wax molds. This manufacturing approach leverages wax loss technology, a highly accurate method that ensures the impeller's dimensional accuracy and surface quality. This combination of materials and manufacturing techniques allows for a comprehensive experimental analysis of the numerical model's predictive capabilities with respect to part-load cavitation instability in high-specific-speed pumps.

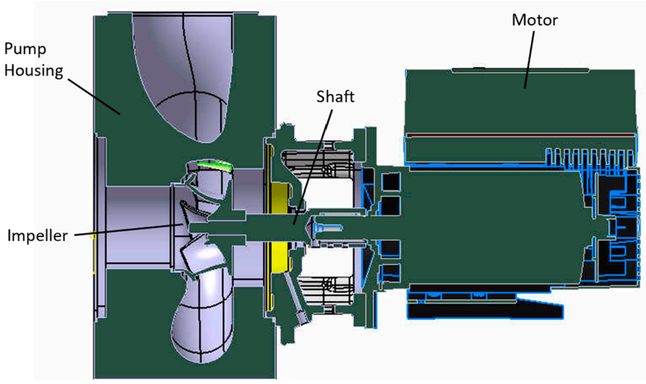

Figure 1. Section view of pump model.

2.2. Test Setup

The outlet flange of the model is DN100, and the inlet flange is DN125. The flow meter is placed on the outlet pipeline. In order to ensure uniform flow, it is kept at a length greater than five times the direct length of the outlet flange with the outlet elbow and outlet valve. The pipeline where the flow meter is placed is inclined by about five degrees to ensure that bubbles do not accumulate at the flow sensor, resulting in larger flow measurement errors.

The test rig has three pressure sensors; one is arranged above the pressure tank to measure the system pressure, another is located at the inlet of the model pump to measure the inlet pressure of the model pump, and the final one is located at the outlet of the model pump to measure the outlet pressure of the model pump (shown in Figure 2). The sensor range is −0.1 mpa–1 mpa, and the accuracy is ±0.3%. The speed sensor is placed directly in front of the pump shaft and used with light-sensitive paper to test the speed of the water pump.

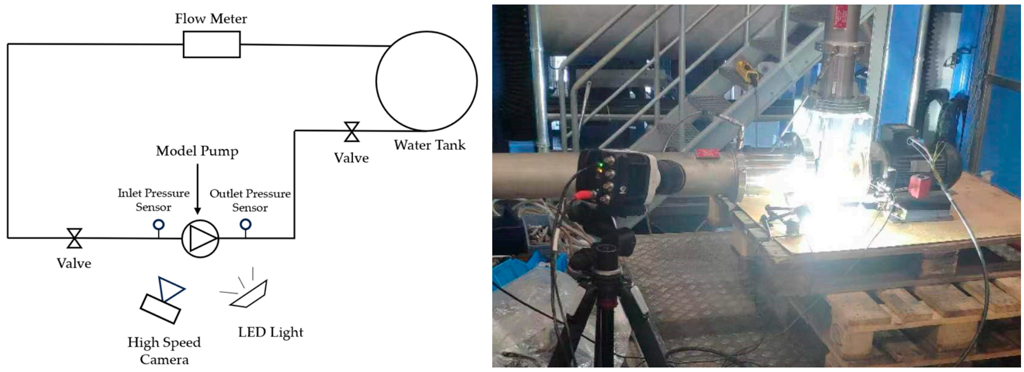

Figure 2. High-speed photography test setup.

This experiment used a Miro LAB 310 high-speed video camera. It has characteristics such as high resolution and ultra-low light sensitivity. The maximum resolution is 1280 × 800, and the recording speed at this time is 3200 fps, with a maximum recording speed of 650,000 fps. The camera is connected to a computer through a gigabit Ethernet for operation.

The light source used in this test is the double-headed version of the Danny u white LED light source. This light source can have a maximum brightness value of 800,000 lux at a distance of 10 cm from the subject, and the light source has no flash frequency, so the photographed material will not be bright or dark.

2.3. Performance Test Results Analysis

The head curve and NPSH curve of the investigated pump model are presented in Figure 3. A meticulous curve analysis reveals the presence of saddle-type instability within the head curve, with its onset occurring precisely at 80% of the pump's rated flow rate. This observation aligns with prior research, which has documented flow instabilities under similar conditions, encompassing phenomena such as inlet recirculation or impeller outlet recirculation.

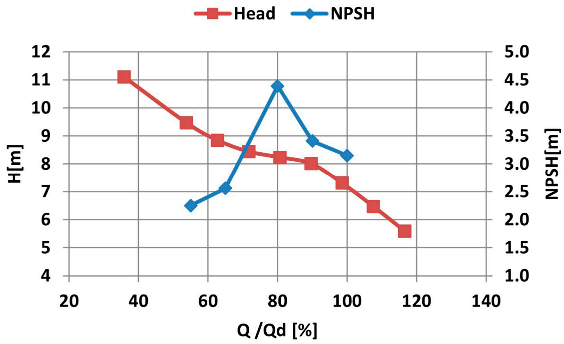

Figure 3. Head and NPSH curve based on test.

To further elucidate the cavitation behavior, a modified head curve was constructed utilizing the non-cavitation head curve as a baseline, with a deliberate 3% reduction in head. This adjustment served as a reference for assessing the pump's performance under slightly compromised conditions. The corresponding NPSH values at each 3% head decrement were acquired through a methodical approach involving constant flow and step-wise depressurization. A comprehensive dataset encompassing five distinct points, spanning from low to high flow rates, was recorded for analysis. Inspection of the NPSH curve depicted in Figure 3 reveals a peak in the $\text{NPSH}_{3\%}$ value at 80% of the rated flow, a point that coincides precisely with the initiation of the saddle-type instability observed in the head curve. At this critical flow rate, the $\text{NPSH}_{3\%}$ attains a maximum value of 4.4 m, representing a significant increase of 1.4 times the NPSH recorded at the pump's rated operating point. This finding underscores the sensitivity of the pump's performance to flow variations in the vicinity of the instability region, highlighting the importance of accurate characterization and mitigation strategies for such instabilities in pump design.

3. Numerical Model

3.1. Mesh Setup

Mesh generation constitutes a pivotal component of numerical simulations, wherein the quality and quantity of meshes directly correlate with the accuracy of the computational outcomes [23,24]. In light of this significance, in the present study, a rigorous mesh independence analysis on the pump model was conducted to ensure the reliability of the simulation results. Specifically, the length, width, and height dimensions of the impeller mesh were carefully defined in accordance with the geometric contours of the impeller (shown in Figure 4). Furthermore, to comprehensively assess the sensitivity of the simulations to mesh variations, four distinct mesh configurations were formulated by systematically adjusting the mesh length, width, and height dimensions (shown in Table 2). This approach aims to determine the optimal mesh configuration that ensures both computational efficiency and simulation accuracy.

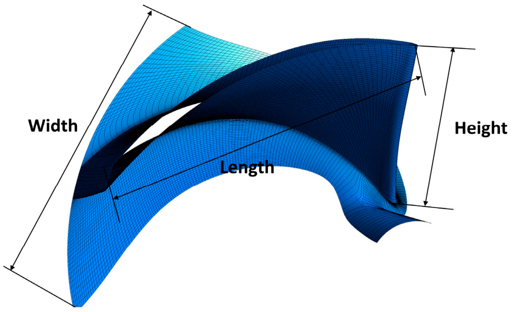

Figure 4. Impeller blade geometry size definition.

Table 2. Mesh independent configurations.

	Baseline	**C1**	**C2**	**C3**
Mesh Quantity	57,776	219,712	869,568	232,926
Length × Width × Height	78 × 42 × 16	100 × 64 × 32	156 × 84 (blade refinement) × 64	100 × 68 (blade refinement) × 32

Baseline is the minimum mesh combination, 78, 42, and 16 meshes in length, width, and height, respectively. The meshes of C1 and C2 are designed according to Formula (1).

$$\mathrm{N} = \mathrm{N}_{\mathrm{n}-1} \times 4 \tag{1}$$

The number of meshes in C1 is approximately four times that of the baseline, and the number of meshes in C2 is approximately four times that of C1. C3 and C1 have similar mesh numbers, but the boundary layer of the blade is encrypted on the basis of C1, which has four layers within 1 mm, so the density of the boundary layer is the same as C2. The mesh scale of the blade cross-section is detailed in the mesh profile in Figure 5. All the meshes in this paper are hexahedron, which are generated by Ansys ICEM 2020 R2.

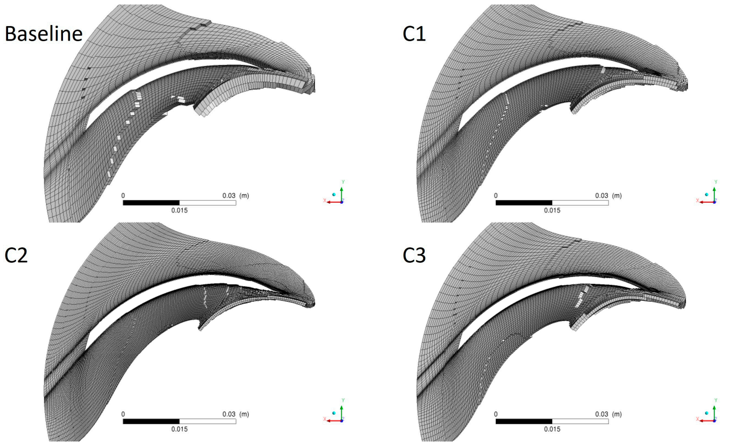

Figure 5. Blade mesh section of four different configurations.

3.2. Boundary Conditions

Despite the inherent complexity of fluid motion, it remains subject to the fundamental principles of mass conservation, momentum conservation, and energy conservation. Within the domain of Newtonian fluids, these governing laws can be mathematically represented by the Navier–Stokes equation. When considering an absolute reference frame expressed in rectangular coordinates, the essential control equations that delineate the fluid's flow state encompass the following:

$$\frac{\partial \rho_m}{\partial t} + \frac{\partial(\rho_m u_j)}{\partial x_j} = 0 \tag{2}$$

$$\frac{\partial(\rho_m u_j)}{\partial t} + \frac{\partial(\rho_m u_i u_j)}{\partial x_j} = -\frac{\partial p}{\partial x_i} + \frac{\partial}{\partial x_i}\left(u_m \frac{\partial u_i}{\partial x_j}\right) \tag{3}$$

In the above two equations, ρ is the liquid density, u is the velocity, p is the pressure, t is the time, x is the spatial coordinate, μ is the dynamic viscosity, and i, j represents the direction component of the coordinate axis and complies with the summation convention in the tensor.

In this part, the k-epsilon turbulence model is used for the solution based on ANSYS CFX 2020 R2. The inlet and outlet boundary conditions are defined as the mass flow inlet and pressure outlet, respectively, the reference pressure is set as the standard atmospheric pressure, and the inlet mass flow is calculated for various working conditions. On this basis, the solid wall surface was defined as a no-slip boundary condition, and the roughness of the wall surface was set to 0.025 mm, which is aligned with the 3D printed impeller surface roughness (shown in Figure 6).

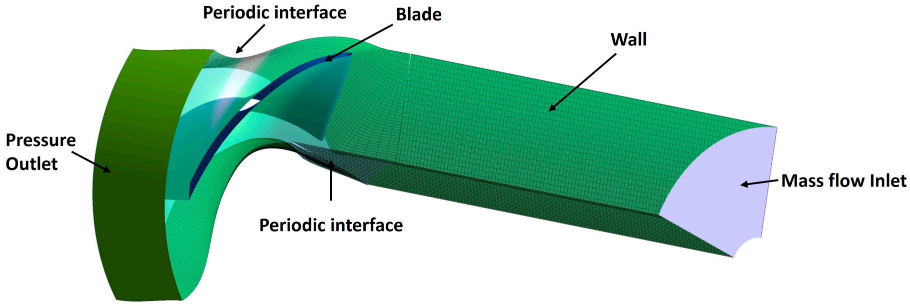

Figure 6. Boundary condition setup.

Physically, cavitation is a fast-phase transition process, and it is difficult to capture the right thermal effects in the numerical simulation. Therefore, a homogeneous model and default Rayleigh–Plesset model were applied to the numerical model. A mixture model was chosen for inter-phase transfer to share the flow-field velocity for two different fluid phases. One was water at 25 °C, and the other was water vapor at 25 °C. The vapor pressure was 3166 Pa.

The simulation was conducted using a steady-state model with a convergence criterion of an RMS residual of 10-5, making the simulation more robust. High resolution was selected for the advection in order to make the results more accurate.

3.3. Mesh Independence Results Analysis

Figure 7 shows the $\mathrm{NPSH}_{3\%}$ curves for four different mesh combinations. Convergence of all the results reached the RMS residual with the 10-5 target. From the analysis of the results, it can be seen that the NPSH peak points of baseline and C1 are the same, both at 65% of the rated flow rate. But the size of the peak varies, and the smaller the mesh scale, the smaller its peak size. It means that by increasing the width, length and height by average, the NPSH peak size will decrease but the NPSH peak position will not change. The NPSH peak points of C2 and C3 are both at 80% of the rated flow rate, which is aligned with the NPSH peak point based on the test shown in Figure 3. A meticulous comparative analysis of configurations C2 and C3, conducted under identical conditions of length (100) and height (32), yet with a subtle alteration in width from 64 to 68 units solely aimed at refining the mesh density within the boundary layer, uncovers a pronounced effect on the NPSH peak points. This influence is not merely limited to the positioning of the peak points; rather, it extends to the magnitude of the peak values as well. It is noteworthy that the scale of other mesh sizes exhibits a comparatively minor effect on the NPSH peak points. This finding underscores the crucial role of mesh refinement in the boundary layer in accurately capturing the dynamics of NPSH peaks, thus enhancing the reliability and accuracy of the numerical simulations.

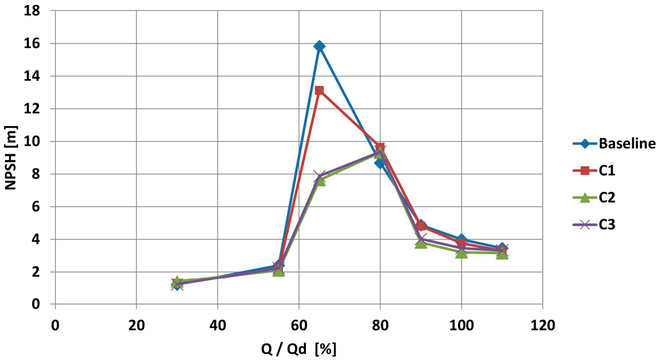

Figure 7. NPSH curves of four different mesh configurations.

The k-epsilon turbulence model implemented in ANSYS CFX employs a scaled wall function, with a $y+$ value commonly ranging from 20 to 200 considered reasonable. Notably, despite further refinement of the mesh to achieve lower $y+$ values, the impact on the simulation results remains marginal. Figure 8 depicts the $y+$ distribution for four distinct mesh configurations. From this figure, it is evident that the $y+$ values for all four mesh scales remain within the acceptable range of 200. However, variations in $y+$ values are observed on the blade suction side and leading edge, as detailed in Table 3. At the leading edge, where the bubble concentration is prominent, a significant difference is observed. Specifically, the $y+$ values for baseline and C1 configurations are approximately 140, whereas those for C2 and C3 are reduced to 80. This variation in $y+$ values at the leading edge likely contributes to the observed differences in NPSH values at this flow condition.

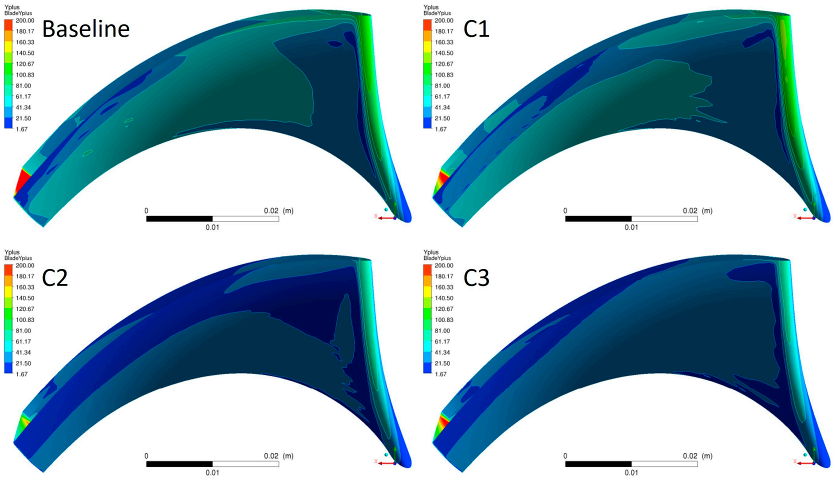

Figure 8. $y+$ distribution of four different mesh configurations.

Table 3. $y+$ on blade surface.

	Baseline	C1	C2	C3
Mesh quantity	57,776	219,712	869,568	232,926
Suction side $y+$	60	60	40	40
Leading edge $y+$	140	140	80	80

Based on the preceding analysis of NPSH peak values, it is recommended that for high-specific-speed pumps, to ensure a stable NPSH peak position, the $y+$ value at the blade's leading edge should be carefully controlled within the range of 20 to 80. This range ensures adequate resolution of the flow dynamics at the critical bubble formation region, thereby improving the accuracy and reliability of the simulation results. Considering time costs and NPSH prediction accuracy, C3 was chosen for subsequent calculations.

3.4. Orthogonal Experimental Design Setup

The Rayleigh–Plesset cavitation model used in this article considers the gasification and condensation processes of bubbles; the equilibrium equation is as follows:

$$R_B \frac{d^2 R_B}{dt^2} + \frac{3}{2}\left(\frac{dR_B}{dt}\right)^2 + \frac{2\sigma}{\rho_f R_B} = \frac{p_v - p}{\rho_f} \tag{4}$$

In the formula, R_B is the radius of the bubble, ρ_f is the density of the liquid medium, and σ is the surface tension coefficient between the liquid and vapor.

p is the pressure of the liquid surrounding the bubble and p_v is the saturated vapor pressure of the liquid medium.

The Zwart cavitation model [25–27] has been refined based on the original Rayleigh–Plesset equation. With the rise in the volume fraction of vapor, the density of vapor nuclei locations diminishes. The Zwart model has revised the volume fraction term in the mass cavitation rate equation, resulting in a new phase transition rate formula.

$$R_e = F_{vap} \frac{3\alpha_{nuc}(1-\alpha_v)\rho_v}{R_B} \sqrt{\frac{2}{3}\left(\frac{p_v - p}{\rho_1}\right)}, p < p_v \tag{5}$$

$$R_c = F_{cond} \frac{3\alpha_v \rho_v}{R_B} \sqrt{\frac{2}{3}\left(\frac{p - p_v}{\rho_1}\right)}, p < p_v \tag{6}$$

α_{nuc} is the volume fraction of vapor core, α_v is the volume fraction of the bubble in the unit volume, F_{vap} is the evaporation coefficient, and F_{cond} is the condensation coefficient.

The evaporation coefficient and condensation coefficient determine the gasification rate and play a key role in the results of pump gasification. Therefore, these two groups of coefficients are defined as the factors of orthogonal experimental design for in-depth study.

In addition to the above two factors, this paper also selected the turbulence model k-epsilon, k-Omega and SST [28] for orthogonal experimental design and selected three different conditions according to the characteristics of these three factors. See Table 4 below for specific conditions. Besides these three factors, the other boundary conditions had the same setup as those in the mesh independence analysis part.

Table 4. Three different factors with three different conditions.

Turbulence Model	Evaporation Coefficient	Condensation Coefficient
k-epsilon	25	0.005
k-Omega	50	0.01
SST	75	0.015

According to the principle of orthogonal experimental design, the L9 (3^4) orthogonal design table is selected as the research method of this numerical simulation. These 9 test points are used to replace 27 test points in order to achieve the same purpose. All 27 intersections of the cube represent 27 test points of the comprehensive experiment, and 9 test points determined by orthogonality are evenly scattered among them. The cube is divided into three planes from either direction, and each plane contains nine intersection points, of which exactly three are the test points arranged by the orthogonal design table. Then, a row segment and a column segment at the middle of each plane are added so that each plane has three equally spaced row segments and column segments, and there is exactly one test point on each row and one test point on each column. It can be seen that the nine test points are evenly distributed. This is the equilibrium of orthogonal experimental design.

According to the contents in Table 4, the L9 (3^4) orthogonal design table can be expressed as follows in Table 5. Column numbers 1, 2 and 3 represent the turbulence model, evaporation coefficient (F_{vap}), and condensation coefficient (F_{cond}), respectively.

Table 5. L9(34) orthogonal design table.

No.	Items		
	1 Turbulence Model	**2 F_{vap}**	**3 F_{cond}**
1	1 (k-epsilon)	1 (25)	1 (0.005)
2	1 (k-epsilon)	2 (50)	2 (0.01)
3	1 (k-epsilon)	3 (75)	3 (0.015)
4	2 (k-Omega)	1 (25)	2 (0.01)
5	2 (k-Omega)	2 (50)	3 (0.015)
6	2 (k-Omega)	3 (75)	1 (0.005)
7	3 (SST)	1 (25)	3 (0.015)
8	3 (SST)	2 (50)	1 (0.005)
9	3 (SST)	3 (75)	2 (0.01)

3.5. Sensitivity Results Analysis

Figure 9 presents the $NPSH_{3\%}$ curve derived from nine groups of orthogonal experimental designs. A detailed analysis of this figure provides insights into the interplay between turbulence models and peak flow characteristics. Specifically, the peak flow points exhibit notable variations across the three turbulence models considered. The k-Omega model exhibits a peak point flow at 55% of the rated flow rate, while the SST model peaks at 65% of the rated flow. Intriguingly, the k-epsilon model exhibits two distinct peak points: one at 65% and another at 80% of the rated flow. In comparing the peak point flows, it is evident that the k-epsilon model's peak flow points align more closely with the tested

NPSH curve. This observation suggests that the k-epsilon turbulence model may offer a more accurate representation of the flow characteristics, particularly in the vicinity of the peak NPSH values. However, further validation and analysis are necessary to confirm this inference and ensure the reliability of the simulation results.

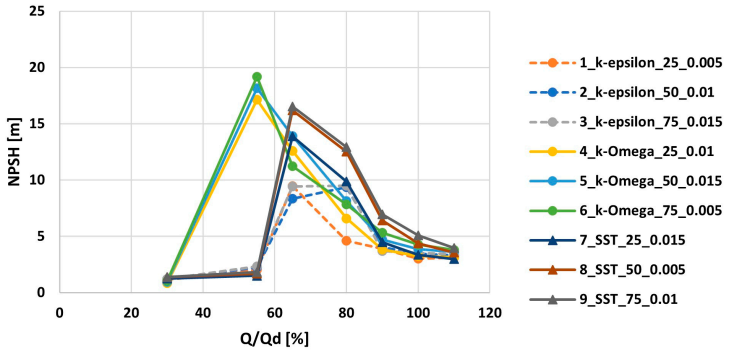

Figure 9. $NPSH_{3\%}$ curve based on orthogonal experimental design.

Figure 10 shows the relationship between the evaporation coefficient and $NPSH_{3\%}$ peak point under different turbulence models. As evident from the plotted curves, the $NPSH_{3\%}$ peak value exhibits a gradual upward trend with an increasing evaporation coefficient. This indicates a positive correlation between the evaporation coefficient and the $NPSH_{3\%}$ peak value. Notably, the slopes of the three curves corresponding to the different turbulence models exhibit minimal variation. Among the three turbulence models, the k-Omega model yields the highest $NPSH_{3\%}$ peak value, whereas the k-epsilon model produces the lowest peak value. This disparity in peak $NPSH_{3\%}$ values highlights the sensitivity of the results to the choice of turbulence model, particularly in scenarios involving evaporation effects.

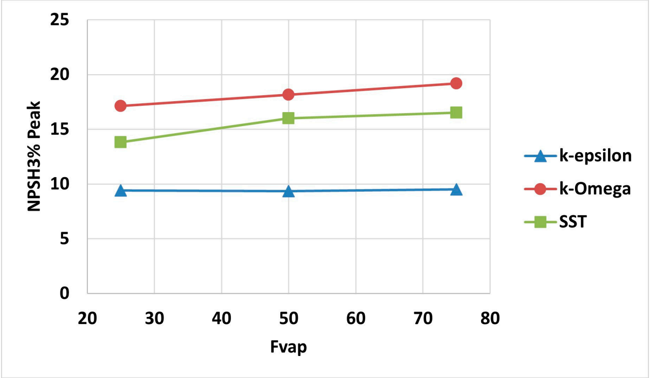

Figure 10. Relationship between vaporization coefficient and $NPSH_{3\%}$ peak with different turbulence models.

Figure 11 shows the relationship between the condensation coefficient and $NPSH_{3\%}$ peak point under different turbulence models. The observed trends vary significantly among the models. For the k-epsilon turbulence model, an increasing condensation coefficient is accompanied by a corresponding increase in the $NPSH_{3\%}$ peak value, suggesting a direct positive correlation. Conversely, under the k-Omega model, when the condensation coefficient reaches 0.01, the $NPSH_{3\%}$ peak value attains its minimum. However, this result is also influenced by the minimum evaporation coefficient. The SST model exhibits a distinct pattern, where the maximum $NPSH_{3\%}$ peak value occurs at an intermediate condensation coefficient of 0.01 and an evaporation coefficient of 75, yielding a value of 16.5 m. Interestingly, comparison with a condensation coefficient of 0.05 and an evaporation coefficient of 50, resulting in a peak value of 16 m, revealed no significant increase.

Since the evaporation coefficient is positively correlated with the peak value of NPSH, the condensation coefficient may be negatively correlated with the peak value of NPSH. That is, the greater the condensation coefficient, the smaller the peak value of $NPSH_{3\%}$.

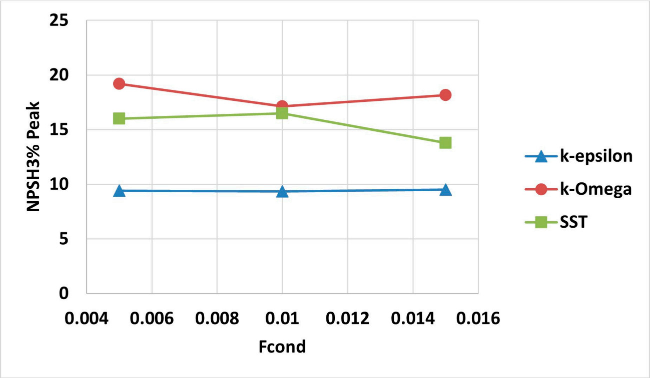

Figure 11. Relationship between condensation coefficient and $NPSH_{3\%}$ peak with different turbulence models.

4. Analysis and Discussion

In this study, the 55% rated flow point (Q55) and NPSH peak flow point (Q80) were selected as benchmarks to compare the computational fluid dynamics (CFD) cavitation contours with high-speed photographic images. Specifically, four sets of high-speed photographic cavitation images, capturing the inception to severe cavitation stages for each flow condition, were chosen. The inlet pressure for the corresponding CFD cavitation contours was set identical to that in the experimental tests.

Based on the sensitivity analysis conducted, it was determined that the turbulence model exerts the most significant influence on the NPSH peak point, followed by the evaporation coefficient, with the condensation coefficient having the least impact. Consequently, the comparison in this paper primarily focused on the turbulence model, which emerged as the most influential factor. To this end, test points 2 from the orthogonal design table were selected for detailed analysis.

4.1. Q55 Flow Point Comparison Analysis

Figure 12 presents the high-speed photographic images of Q55 under different inlet pressures. Figure 13 presents the CFD cavitation contours and pressure contours of Q55 under different inlet pressures.

Utilizing high-speed photography techniques, a definitive observation was made regarding the onset of cavitation, which emerged for the first time at an $NPSH_a$ of 5.55 m. This cavitation was found to be localized and minimal, primarily confined to the mid-section of the blade leading edge, occupying approximately two-fifths of the distance from the hub plate to the shroud plate. This spatial distribution concurred precisely with the CFD simulations, reinforcing the predictive accuracy of the numerical model. Notably, concurrent with this cavitation initiation, a distinct region within the pressure cloud imagery exhibited pressures below the vaporization threshold of 3166 Pa, precisely at the leading edge midpoint, elucidating the underlying mechanism for cavitation manifestation in this specific area. At a reduced $NPSH_a$ of 3.25 m, pronounced recirculation cavitation was discernible at the inlet, characterized by a lateral triangular shape in the blade's cavitation area. This geometric configuration mirrored both the CFD-predicted cavitation contour and the low-pressure region depicted in the pressure cloud map, further validating the correspondence between experimental observations and computational predictions.

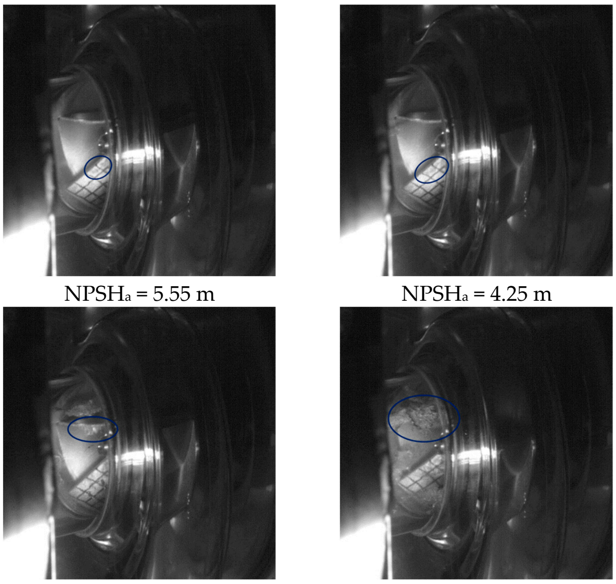

NPSH$_a$ = 5.55 m NPSH$_a$ = 4.25 m

NPSH$_a$ = 3.25 m NPSH$_a$ = 2.25 m

Figure 12. Q55 high-speed photographic images with different inlet pressures.

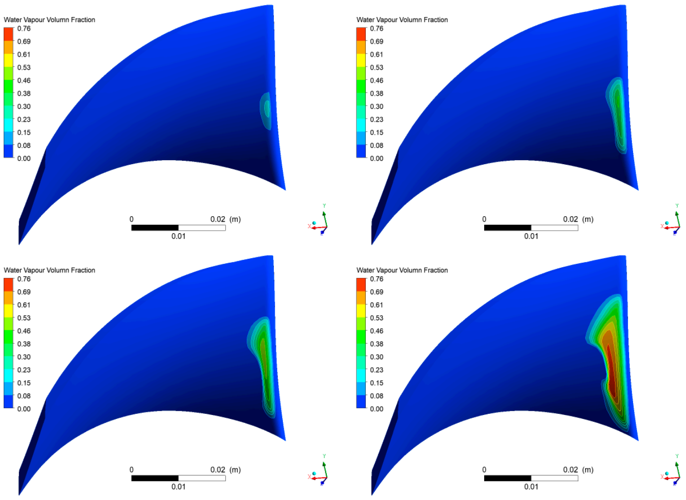

(**a**) Cavitation contour

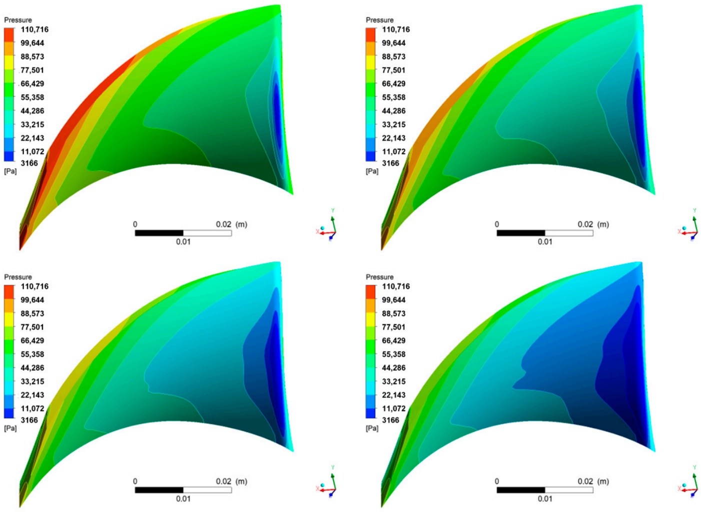

(**b**) Pressure contour

Figure 13. Q55 cavitation contours and pressure contours with different inlet pressures.

As the test pressure continued to decline, the visual resolution of the blade surface cavitation morphology became increasingly challenging due to the exacerbation of inlet recirculation cavitation. Consequently, direct comparison with the CFD cavitation counters became impractical. Nevertheless, a discernible trend emerged: the low-pressure cavitation zone progressively encompassed the entire leading edge, gradually transitioning from a localized phenomenon to a more pervasive state that harmoniously aligned with the high-speed photography records.

As depicted in Figure 14, the variation in Q55 water vapor fraction and pressure at the 0.4 span location on the impeller suction side is analyzed under varying inlet pressures. A comprehensive data comparison reveals a distinct trend: as the inlet pressure decreases, there is a gradual decline in the overall pressure distribution across the suction surface. Concurrently, the region where pressures fall below the vaporization threshold of 3166 Pa expands significantly, indicative of an intensifying cavitation phenomenon. Specifically, the maximum water vapor fraction, a quantitative measure of cavitation intensity, escalates from an initial value of 0.18 to a pronounced level of 0.719 at an NPSH$_a$ of 2.25 m. Furthermore, the ratio of cavitation extent along the streamwise direction also exhibits a notable rise, from 0.01 to 0.06, indicating a more widespread and persistent cavitation pattern as inlet pressure deteriorates.

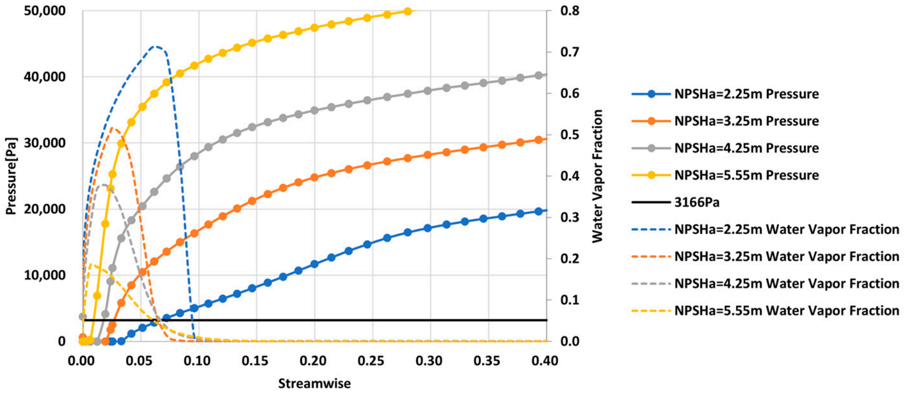

Figure 14. Q55 water vapor fraction and pressure at impeller 0.4 span location.

4.2. NPSH Peak Flow Point Comparison Analysis

Figure 15 presents the high-speed photographic images of Q80 under different inlet pressures. Figure 16 presents the CFD cavitation contours and pressure contours of Q80 under different inlet pressures.

Through observation, it is found that the cavitation inception of Q80 is earlier than that of Q55. Specifically, at an NPSH$_a$ of 7.89 m, a minute yet discernible cavitation region emerges proximal to the shroud plate at the leading edge, exhibiting a slender morphology. The corresponding pressure contour concurs, indicating that this region coincides with the area where pressures fall below the vaporization threshold, spanning approximately half of the inlet edge. As the inlet pressure progressively diminishes, the cavitation area experiences a gradual yet steady expansion, encroaching upon the hub region. At an NPSH$_a$ of 4.39 m, the cavitation zone assumes a semi-elliptical shape, a characteristic indicative of typical sheet cavitation as evidenced by photographic imagery. Furthermore, no indications of unstable flow phenomena, such as rotating cavitation, are observed at this stage. Upon further pressure reduction to an NPSH$_a$ of 2.39 m, the entire blade leading edge becomes inundated with cavitation. This extensive cavitation area is found to be in good agreement with the cavitation contours predicted by CFD simulations. An examination of the pressure contours reveals a pronounced trend towards the further development of cavitation towards the suction surface in close proximity to the shroud plate.

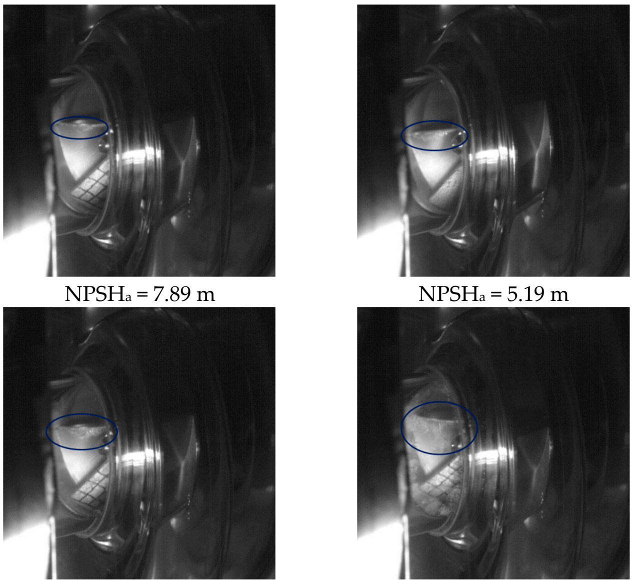

NPSH$_a$ = 7.89 m NPSH$_a$ = 5.19 m

NPSH$_a$ = 4.39 m NPSH$_a$ = 2.39 m

Figure 15. Q80 high-speed photographic images with different inlet pressures.

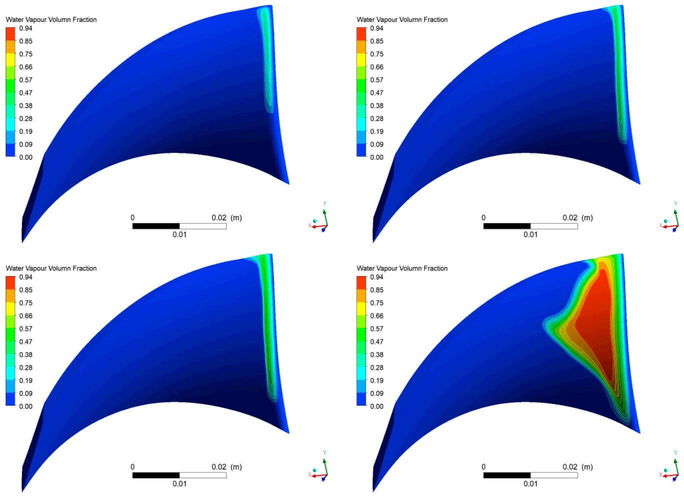

(**a**) Cavitation contour

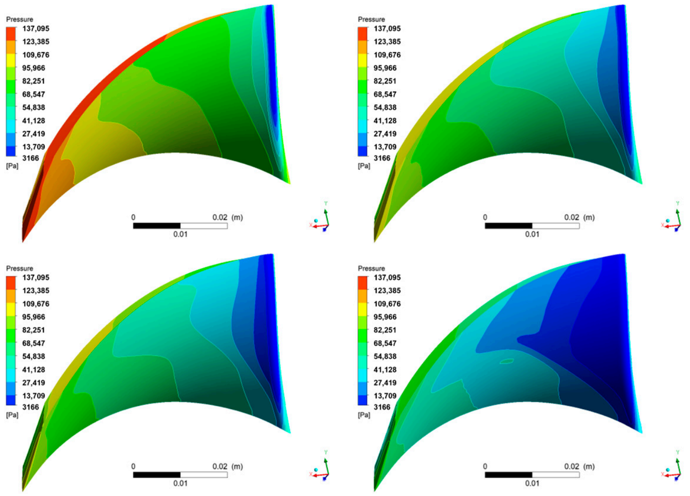

(**b**) Pressure contour

Figure 16. Q80 cavitation contours and pressure contours with different inlet pressures.

Figure 17 presents water vapor fraction and pressure distribution on the suction side of the Q80 impeller at a 0.5 span location, under varying inlet pressure conditions. Analogous to the Q55, a discernible trend emerges where the overall pressure on the suction surface undergoes a gradual decline as the inlet pressure decreases. Concurrently, the region where pressures fall below the vaporization threshold of 3166 Pa expands progressively, accompanied by a significant increase in the maximum water vapor fraction. Specifically, this fraction escalates from an initial value of 0.27 to a peak of 0.94 at an $NPSH_a$ of 2.39 m. However, a notable distinction arises when comparing the behavior of Q80 with that of Q55. At the peak water vapor volume fraction, attained at an $NPSH_a$ of 2.39 m, the Q80 does not exhibit a rapid decline in the vapor fraction as observed in Q55. Instead, the vapor fraction remains elevated, maintaining a high value until it gradually tapers off to approximately 0.3 further downstream in the streamwise direction. This prolonged persistence of high vapor fractions underscores the severe development of sheet cavitation in the Q80 configuration.

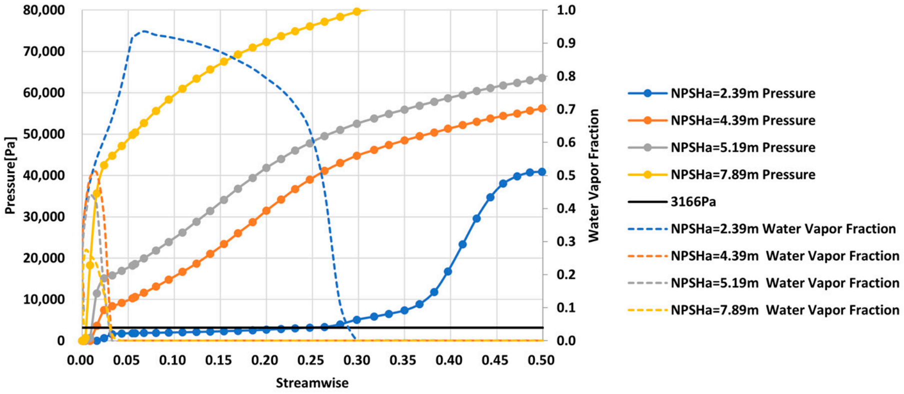

Figure 17. Q80 water vapor fraction and pressure at impeller 0.5 span location.

4.3. Discussion

Based on a rigorous comparative analysis of numerical simulations and experimental data in the aforementioned flow conditions, it was established that the positioning and morphology of the cavitation region, as predicted by the k-epsilon turbulence model in conjunction with an evaporation coefficient of 50 and a condensation coefficient of 0.01, under varying flow rates, closely align with the actual high-speed photographic patterns. This numerical simulation approach, when coupled with an optimal grid count at the impeller inlet leading edge, demonstrates a remarkable capability in accurately simulating the flow regime wherein the NPSH peak occurs at 80% of the rated flow point, thereby validating its consistency with experimental findings.

However, a minor limitation is discernible in that the predicted NPSH peak value by the model tends to be slightly overestimated, necessitating further refinement and enhancement. Nonetheless, the overarching significance of this simulation strategy lies in its potential to serve as a solid foundation for optimizing the design of high-specific-speed pumps operating at part-load conditions, particularly in mitigating cavitation instability. This discovery underscores the value of such numerical methods in advancing the field of pump design and performance optimization.

5. Conclusions

1. The mesh independence analysis conducted in this study reveals a pivotal role of the mesh point density in the boundary layer for the NPSH peak. It significantly influences both the location and magnitude of the NPSH peak. When the leading edge $y+$ is set to 80, the NPSH peaks emerge at a rated flow rate of 80%, which is aligned well with the experimental observations. Therefore, it is imperative to maintain the $y+$ value of the leading edge in a high-specific-speed centrifugal pump within the range of 20 to 80

to ensure a stable NPSH peak position. Furthermore, our analysis indicates a negative correlation between the mesh size and NPSH value, which means that the larger the mesh size, the larger the NPSH value.

2. Upon performing a sensitivity analysis through orthogonal experimental design on the three key factors, it becomes evident that the turbulence model exerts the most significant influence on the NPSH peak value. Following the turbulence model, the evaporation coefficient plays a secondary role, while the condensation coefficient has the least impact. Notably, a positive correlation exists between the evaporation coefficient and the NPSH peak value, implying that an increase in the evaporation coefficient leads to a higher NPSH peak value. Conversely, the condensation coefficient exhibits a negative correlation with the $\mathrm{NPSH}_{3\%}$ peak value, indicating that a lower condensation coefficient results in a higher NPSH peak value.

3. Based on a comparative analysis of numerical simulations and experimental results across various flow rates, rotating cavitation and sheet cavitation were found under partload conditions at Q55 and Q80. It was also observed that the shape and size of cavitation bubbles predicted by the k-epsilon turbulence model, combined with an evaporation coefficient of 50 and a condensation coefficient of 0.01, exhibit a close correlation with actual high-speed photography observations. Consequently, the pivotal parameters for the numerical modeling of cavitation in high-specific-speed pumps operating under part-load conditions are identified as the k-epsilon turbulence model, an evaporation coefficient of 50, a condensation coefficient of 0.01, and a boundary layer with a $y+$ value ranging from 20 to 80 at the leading edge. The establishment of this numerical model, incorporating these crucial parameters and boundary conditions, offers a viable approach for further investigations into part-load cavitation instability optimization in high-specific-speed pumps.

Author Contributions: Conceptualization, Z.S.; methodology, Z.S.; software, J.Z.; investigation, C.W.; resources, J.Z.; test, R.L. and S.Q. All authors have read and agreed to the published version of the manuscript.

Funding: This research was supported by Zhejiang Provincial Natural Science Foundation of China under Grant No. LY24E090004, Taizhou Science and Technology Plan Project under Grant No. 23gya15, and LEO Group Postdoctoral Program.

Data Availability Statement: The relevant data can be found in this article.

Conflicts of Interest: Authors Shijun Qiu and Rong Lin were employed by the company Leo Group Pump (Zhejiang) Co., Ltd. The remaining authors declare that the research was conducted in the absence of any commercial or financial relationships that could be construed as a potential conflict of interest.

References

1. Kosyna, G.; Schmidt, T.H.; Wulff, D.; Spohnholtz, H.H. NPSHR of Mixed-Flow Pumps at Part-Load Operating Conditions. In Proceedings of the 1995 International Symposium on Cavitation, Deauville, France, 2–5 May 1995.
2. Gulich, J.F. Partload operation, impact of 3-D flow phenomena performance. In *Centrifugal Pumps*; Springer: Berlin/Heidelberg, Germany; New York, NY, USA, 2008; pp. 200–205.
3. Friedrichs, J.; Kosyna, G. Experimental and Numerical Investigation of the Performance Instability in a Mixed-Flow Pump. In *2002 Proceedings of ASME FEDSM*; ASME: Montreal, QC, Canada, 2002.
4. Deng, Y.X.; Li, R.N.; Han, W. Characteristics of backflow vortex cavitation in screw centrifugal pump. *Trans. Chin. Soc. Agric. Eng.* **2015**, *31*, 86–90.
5. Deng, Y.X.; Li, R.N.; Han, W. Unsteady vortex cavitation in a screw centrifugal pump. *J. Huazhong Univ. Sci. Technol. (Nat. Sci. Ed.)* **2014**, *42*, 118–121.
6. Deng, Y.X.; Li, R.N.; Han, W. Evaluation and analysis of vortex cavitation in impeller region of screw centrifugal pumps. *J. Lanzhou Univ. Technol.* **2015**, *41*, 55–58.
7. Chen, Q. Study on Unsteady Flow and Cavitation Characteristics of Centrifugal Pump under Low Flow Condition. Master's Thesis, Xi'hua University, Chengdu, China, 2022.
8. Li, H.; Shen, Z.H.; Nicholas, P. Experimental and unsteady numerical research of a high-specific-speed pump for part-load cavitation instability. *Adv. Mech. Eng.* **2019**, *11*, 168781401982893. [CrossRef]

9. Fu, Y.X.; Yuan, S.Q.; Yuan, J.P. Effect of Blade Numbers on Cavitating Flow of Centrifugal Pump under Low Flow Rates. *Trans. Chin. Soc. Agric. Mach.* **2015**, *46*, 21–27.
10. Fu, Y.X. Study on Dynamic Instability and Cavitation Characteristics of Turbopump and Induced Rotation. Ph.D. Thesis, Jiangsu University, Zhenjiang, China, 2014.
11. Fu, Y.X.; Yuan, S.Q.; Yuan, J.P. Internal flow characteristics of centrifugal pump at low flow rates. *J. Drain. Irrig. Mach. Eng.* **2014**, *32*, 185–190.
12. Yuan, J.P.; Fu, Y.X.; Yuan, S.Q. A Study of Cavitation Flow in a Centrifugal Pump at Part Load Conditions Based on Numerical Analysis. In Proceedings of the ASME 2012 Fluids Engineering Division Summer Meeting Collocated with the ASME 2012 Heat Transfer Summer Conference and the ASME 2012 10th International Conference on Nanochannels, Microchannels, and Minichannels, Rio Grande, OH, USA, 8–12 July 2012.
13. Li, X.J.; Yuan, S.Q.; Pan, Z.Y. Numerical simulation of leading edge cavitation within the whole flow passage of a centrifugal pump. *Sci. China (Technol. Sci.)* **2013**, *56*, 2156–2162. [CrossRef]
14. Fu, Y.X.; Yuan, J.P.; Yuan, S.Q. Numerical and experimental analysis of flow phenomena in a centrifugal pump operating under low flow rates. *J. Fluids Eng.* **2015**, *137*, 011102. [CrossRef]
15. Yuan, J.P.; Hou, J.; Fu, Y.X. A study on the unsteady characteristics of the backflow vortex cavitation in a centrifugal pump. *J. Vib. Shock.* **2018**, *37*, 24–30.
16. Cui, B.L.; Zhang, Y.B.; Huang, Y.K. Analysis of the pressure pulsation and vibration in a low-specific-speed centrifugal pump. *J. Fluids Eng.* **2021**, *143*, 021201. [CrossRef]
17. Feng, J.J.; Ge, Z.G.; Yang, H.H. Rotating stall characteristics in the vaned diffuser of a centrifugal pump. *Ocean. Eng.* **2021**, *229*, 108955. [CrossRef]
18. Li, Y.; Li, X.J.; Zhu, Z.C. Investigation of unsteady flow in a centrifugal pump at low flow rate. *Adv. Mech. Eng.* **2016**, *8*, 1687814016682151. [CrossRef]
19. Zhang, N.; Gao, B.; Ni, D. Coherence analysis to detect unsteady rotating stall phenomenon based on pressure pulsation signals of a centrifugal pump. *Mech. Syst. Signal Process.* **2021**, *148*, 107161. [CrossRef]
20. Zhou, P.J.; Wang, F.J.; Mou, J.G. Investigation of rotating stall characteristics in a centrifugal pump impeller at low flow rates. *Eng. Comput.* **2017**, *34*, 1989–2000. [CrossRef]
21. Alavi, A.; Roohi, E. Large eddy simulations of cavitation around a pitching-plunging hydrofoil. *Phys. Fluids* **2023**, *35*, 125102. [CrossRef]
22. Mousavi, S.M.; Roohi, E. On the effects of hybrid surface wettability on the structure of cavitating flow using implicit large eddy simulation. *J. Taiwan Inst. Chem. Eng.* **2023**, *148*, 104828. [CrossRef]
23. Ravi, B.; Eugene, S.; Simon, B. Influence of impeller leading edge profiles on cavitation and suction performance. In Proceedings of the Twenty-Seventh International Pump Users Symposium, Doha, Qatar, 17–20 March 2012.
24. Wack, J.; Riedelbauch, S. Numerical simulations of the cavitation phenomena in a Francis turbine at deep part load conditions. In Proceedings of the Ninth International Symposium on Cavitation, Lausanne, Swiss, 6–10 December 2015.
25. Bakir, F.; Rey, R.; Gerber, A.G. Numerical and experimental investigations of the cavitating behavior of an inducer. *Int. J. Rotating Mach.* **2004**, *10*, 15–25. [CrossRef]
26. Zwart, P.J.; Andrew, A.G.; Belamri, T. Two-phase flow model for predicting cavitation dynamics. In Proceedings of the ICMF 2004 International Conference on Multiphase Flow, Yokohama, Japan, 30 May–3 June 2004.
27. Coutier, D.O.; Fortes, P.R.; Reboud, J.L. Evaluation of the turbulence model influence on the numerical simulations of unsteady cavitation. *J. Fluids Eng.* **2003**, *125*, 38–45. [CrossRef]
28. Wang, F.J. Three-dimensional turbulence model and its application in CFD. In *Computational Fluid Dynamics Analysis*; Tsinghua University Press: Beijing, China, 2004; pp. 113–118.